

ARTICLE OPEN



Mechanism elucidation and scaling control in membrane distillation using 3D printed carbon nanotube spacer

Seongeom Jeong¹, Boram Gu², Sanghun Park³, Kyunghwa Cho⁴, Alicia Kyoungjin An⁵ and Sanghyun Jeong¹

Membrane scaling is a barrier to membrane distillation (MD). In this study, 3D-printed carbon nanotube (CNT) spacer was used to investigate its capability for mitigating membrane scaling during MD and to elucidate the scaling mechanism experimentally and theoretically. CNT spacer was tested under temperature-dependent calcium sulfate scaling conditions, and optical coherence tomography (OCT) and scanning electron microscopy (SEM) were used to measure scaling quantitatively. CNT spacer exhibited unique membrane scaling mechanism, where only a 37% reduction ($29 \text{ Lm}^{-2}\text{h}^{-1}$) in the initial flux was achieved, even above a volume concentration factor (VCF) of 4. On the other hand, the membrane with a polylactic acid (PLA) spacer (controls) entirely lost flux before reaching a VCF of 3.5. Interestingly, bubble formation was observed in CNT spacer, which could be attributed to the enhanced flux and vaporization rate on membrane surface in the presence of rough-surfaced CNT spacer. Bubbly flow along the membrane channel with CNT spacer can potentially reduce surface scaling on membrane during MD. Moreover, due to the surface roughness of CNT spacer, the initial nuclei might be detached more easily from CNT spacer surface than from smooth PLA surface and grow further into larger crystals in the bulk, resulting in reduced dissolved solutes in the solution. This phenomenon was indirectly corroborated by comparing the experimentally measured fluxes and theoretically computed values from our mechanistic model of MD-crystallization developed in this study. Therefore, this study revealed that CNT spacer with rough surfaces can potentially have benefit of mitigating membrane scaling during MD.

npj Clean Water (2023)6:80; <https://doi.org/10.1038/s41545-023-00296-0>

INTRODUCTION

Membrane distillation (MD) is a desalination technology that involves the simultaneous transfer of heat and mass through a hydrophobic membrane. Hence, concentration and temperature polarizations (CP and TP) occur together near the membrane, resulting in the deterioration of MD performance, which is the main issue for its operation^{1–4}. CP and TP in MD mutually influence each other; an increased concentration near the membrane lowers the effective vapor pressure difference between the membrane surface on the feed side and the permeate side, which is the driving force of MD^{1,2,5–7}. CP may further lead to membrane fouling by accumulating a high concentration of foulants on the surface, which aggravates TP on the membrane. For high-rejection membrane processes such as MD, which can theoretically reject all substances except volatile ones, CP inherently occurs at the membrane/solution interface and is caused by the separation of non-volatile species through the membrane. Hence, substances excluded by the membrane can become to act as foulants^{8–10}.

In MD, scaling is generally caused by the formation and deposition of inorganic crystals on the membrane surfaces. Among these, calcium sulfate (CaSO_4) is the main scalant because of its high content in water and low solubility¹¹. It can be formed by both surface and bulk crystallization depending on the CP effect and solubility limitations in the membrane surface and feed solution. The crystals formed can block the membrane pores, reduce the membrane performance (e.g., dramatic flux decline), and further cause membrane wetting^{12,13}, eventually resulting in the loss of membrane performance. Christie et al.¹⁴ observed that the permeate flux decreased by >80% during the first 200 min of

MD operation, as crystals generated in the bulk adhered to the membrane surface and small crystals formed on the surface grew into large crystals that completely blocked the membrane pores. A decrease in the liquid entry pressure was also observed as the scalants covered the membrane surface, resulting in hydrophobicity reduction, and the membranes became partially or fully wet. Therefore, many researchers have studied methods for controlling membrane scaling on MD membranes. For example, chemicals have been injected to lower the feed pH to prevent scalant formation¹² or to disperse the formed scaling (i.e., anti-scalant)^{13,15}. In addition, studies have been conducted to increase membrane hydrophobicity and prevent scalant deposition on membranes¹⁶. However, scaling accompanies various complex and interrelated physical and chemical phenomena affected by membrane properties, which challenges the transparent explanation of their interplay. Furthermore, a high dose of chemicals for scaling mitigation increases the economic and environmental burdens, including an increase in operational costs and the need for further treatment of sludge or wastewater generated during scaling control. Most importantly, the methods studied thus far have been thought to be ineffective in controlling membrane scaling in the long run¹⁷.

Feed spacers are typically used to suppress the formation of the boundary layer between the bulk and membrane surfaces by polarization effects in the MD process^{18,19}. In our previous study²⁰, carbon nanomaterial (graphene and carbon nanotube (CNT))-embedded feed spacers effectively were shown to decrease polarization effects and increase the mean permeate flux (MPF) and ion rejection efficiency (IRE) during MD operation owing to

¹School of Civil and Environmental Engineering, Pusan National University, Busan 46241, Republic of Korea. ²School of Chemical Engineering, Chonnam National University, Gwangju 61186, Republic of Korea. ³Department of Environmental Engineering, Pukyong National University, Busan 48513, Republic of Korea. ⁴School of Civil, Environmental and Architectural Engineering, Korea University, Seoul 02841, Republic of Korea. ⁵School of Energy and Environment, City University of Hong Kong, Tat Chee Avenue, Kowloon, Hong Kong. ✉email: boram.gu@jnu.ac.kr; sh.jeong@pusan.ac.kr

their multiscale roughness. CNTs have received attention as materials for application in membranes because of their excellent mechanical and electrical properties as well as their ability to conduct electricity and heat^{21–24}. In particular, the heat stability and transfer properties of the CNT improved the MD membrane performance. The atomic-scale smoothness and chemical inertness of CNT are reported to play critical roles in their molecular transport through membranes^{23,25}. Moreover, CNT can generate nanoscale pores and improve the membrane hydrophobicity. According to Humoud et al.²⁶, CNT can reduce scale formation on the membrane surface during the MD process and enhance the washability and reversibility of scaling. CNT can also increase the membrane surface roughness^{27,28}, which enhances turbulence and improves convective heat transfer²⁹. Since the spacer is already recognized as a turbulence promoter as well as a polarization effect inhibitor, it is also expected that increasing spacer roughness by introducing CNT might help improve MD efficiency. However, to date, there have been few studies on CNT-embedded spacers, one of which was our previous study²⁰ that confirmed the ability of CNT-embedded spacers to improve MD performance.

This study investigates CaSO_4 scaling, one of the most common scalants in MD operations. The scaling mitigation using the CNT-embedded spacers was experimentally examined, and it was attempted to explain the observed scaling mitigation both experimentally and theoretically; additional experiments were designed to identify the main cause of the scale mitigation in the CNT spacer, and then a mechanistic modeling of crystallization present within the MD system was undertaken to further provide an elucidation of the scaling mechanism. We used a direct-contact membrane distillation (DCMD) testing unit (Fig. 1), and the progression of membrane scaling was monitored in terms of flux decline over time during the MD process. The contaminated membranes were further characterized by scanning electron microscopy (SEM). To better understand real-time scaling trends during the MD operation with or without a CNT-embedded spacer, optical coherence tomography (OCT) was also used.

RESULTS AND DISCUSSION

Scaling behavior of DCMD with CNT-embedded spacer

Long-term permeate flux measurements are essential for determining the effect of scaling on MD membranes. In long-term MD operations with high concentrations, the polarization effects become severe, resulting in membrane scalant deposition or accumulation on the membrane surface. In some cases, scalants were found in the membrane pores. With scaling and an increase in the VCF, the permeate flux decreases^{14,30}. In this study, tests were conducted to examine the effects of the spacer on the permeate flux over a VCF with a CaSO_4 feed solution of 0.01 M

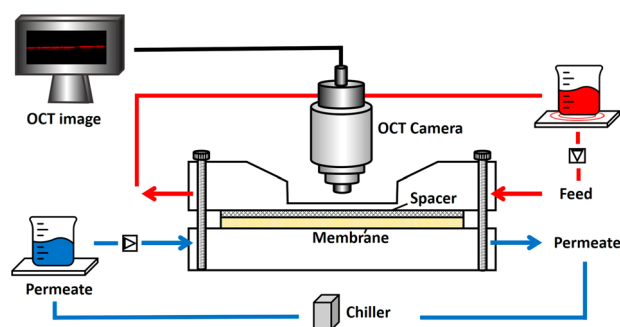


Fig. 1 A schematic of DCMD test unit equipped with OCT device. The DCMD process is operated by observing cross-section of the membrane in real time through an OCT device.

initially. The reported fluxes were obtained from five repeated tests to ensure their representativeness.

Figure 2a shows the results of the flux pattern for different feed temperatures (60, 70, and 80 °C) and spacer types. When the membrane was used without a spacer at 60 °C, the initial permeate flux was 28 LMH. However, it decreased sharply after a VCF of 1.9. Then, the flux was completely lost at a VCF of 2.4, possibly due to membrane pore blocking by membrane scaling. Using the PLA spacer, the permeate flux was maintained at 42 LMH from VCF 1.0 to 2.3, and then the permeate flux started to decline gradually until VCF 3.1. After VCF 3.1, it dropped sharply. These two cases of no-spacer and PLA spacer exhibited similar flux-drop patterns. This implied that the PLA spacer could increase the permeate flux but could not inhibit scaling formation on the membrane. On the other hand, the CNT spacer showed a much higher initial flux than the PLA spacer because of the multiscale roughness of the spacer surface generated by the CNT²⁰. When the CNT spacer was used, the permeate flux reached up to 46 LMH and remained almost constant from VCF 1.0 to 3.0 and then dropped rather slowly after VCF 3.0 and onwards, with a flux still higher than 29 LMH, till VCF 4.0. This showed that the CNT spacer was able to delay the flux decline, possibly by effectively alleviating the polarization effects and controlling CaSO_4 scaling. In the CNT spacer, the flux is maintained high (>20 LMH) until the end of the test. It is clearly shown that the declining trend of permeate water flux due to scale formation was distinguished in the CNT spacer compared to the no-spacer and PLA spacer cases.

The result of feed temperature at 70 °C was compared with that of 60 °C; both the overall flux and flux decline rate were increased. For no-spacer and PLA spacer cases, the fluxes dropped rapidly after VCF 1.7 and 2.1, respectively, while the CNT spacer exhibited a gradual flux decline after VCF 2.1 and then stayed at a flux higher than 58 LMH till VCF 4.0. This implied that the feed temperature affected the flux, and consequently, the rate of concentration was increased by a high flux, causing the scalant to rapidly attach to the membrane surface (Supplementary Fig. 1 in Supplementary Information). Although the solubility of CaSO_4 decreases with increasing temperature, an increase in water flux is primarily due to an increase in vapor pressure, thereby increasing the driving force for vapor permeation. Also the initial concentration is 0.01 M $\text{CaSO}_4 \cdot 2\text{H}_2\text{O}$, which is below the solubility limit in the studied temperature range³¹. This means that the discrepancy in water flux at the same temperature for different spacers could be mainly attributed to different spacer characteristics. The result of feed temperature 80 °C demonstrated that the flux and flux drop timing were shown to be the highest and fastest. This is because the formation of the CaSO_4 scale is accelerated at high temperatures with fast water loss³². An interesting finding is that the CNT spacer demonstrated a different flux decline behavior compared to the no-spacer and PLA spacer cases; a sharp flux drop took place at a flux of >95 LMH, and then the flux was maintained at a constant flux (around 30 LMH) without a complete flux drop. Also, it means that the CNT spacer can maintain a constant flux without completely covering the membrane pores, even if scaling progresses. The promising findings suggest that the presence of the CNT spacer altered the scale formation process and effectively prevented the membrane pores from becoming completely blocked.

Figure 2b shows the flux results, starting at the same initial flux for each spacer in combination with three different temperatures. By comparing these results at different temperatures but with the same initial flux, the impact of the drag force towards the membrane surface on scaling at the initial phase of MD operation was eliminated. To force the initial fluxes in the no-spacer and PLA spacer to be comparable to that of CNT (~46 LMH), feed temperatures were set differently at 65 and 80 °C for the no-spacer and PLA spacer, respectively. While the CNT spacer maintained a flux >29 LMH until VCF 4.5, the fluxes of the PLA spacer and without spacer started to decrease after VCF 2.2 and 1.4, respectively. This

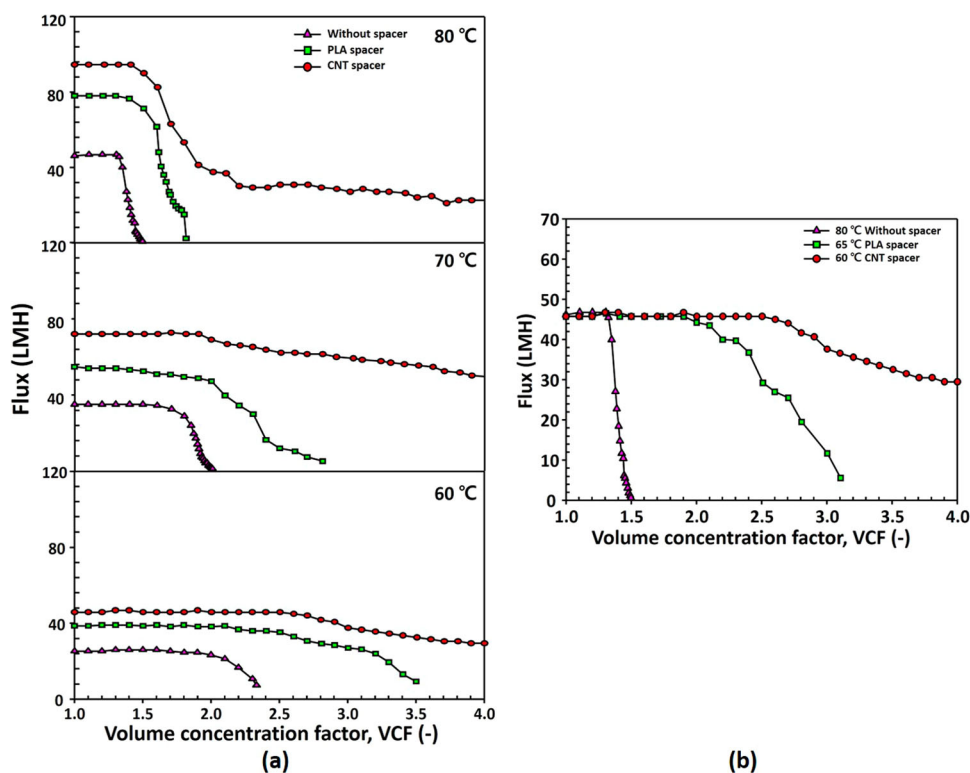


Fig. 2 Effect of CaSO_4 scaling on permeate flux of membrane distillation (MD) operation with different feed spacers in the function of volume concentration factor (VCF). **a** feed temperature 60, 70, and 80 °C. **b** same initial flux. Feed and permeate flow rates were 0.5 liter per minute (LPM), and the concentration of feed solution was 0.01 M CaSO_4 . Feed and permeate temperatures were 60, 65, and 80 °C, and 19.5 °C, respectively.

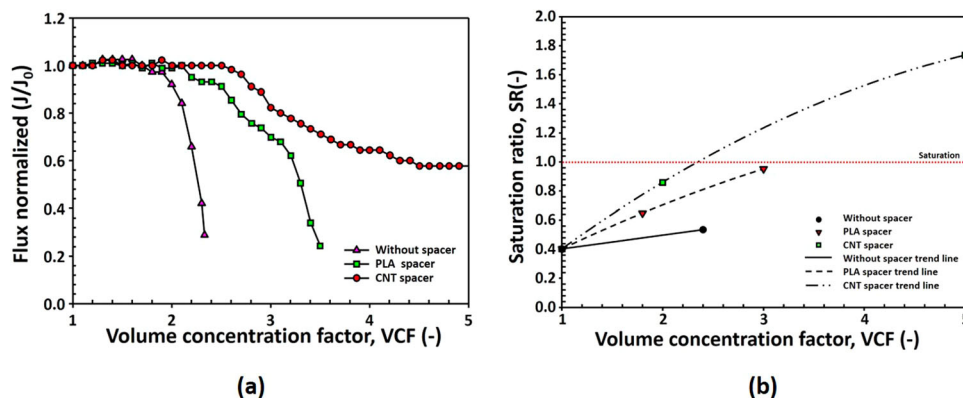


Fig. 3 Effect of CaSO_4 scaling on permeate flux of membrane distillation (MD) operation with different feed spacers. **a** The function of volume concentration factor (VCF) on flux normalized, and **b** saturation ratio (SR). The flow rates of feed and permeate were 0.5 LPM and the concentration of feed solution was 0.01 M CaSO_4 . Feed and permeate temperatures were 60 °C and 19.5 °C, respectively.

result indicated that when the initial concentration rates were the same, the membranes with and without the PLA spacer might be fully covered by scaling and lose their performance after feed concentration becomes 1.4 and 2.2 times its initial value, respectively. In contrast, the use of the CNT spacer reduced the initial flux by 37%, even though the feed concentration was approximately quadrupled. Therefore, it can be concluded that the CNT spacer can retard scaling compared to the PLA spacer, even at the same concentration rate.

Figure 3a shows the results of flux normalization at 60 °C, which can be used to compare the performances of different membranes or conditions, as the absolute flux can be influenced by factors such as the driving force and flow rate. Figure 3b shows the results of comparing the saturation ratio (SR), which is an approximate indication of the degree of calcium saturation. When

the SR is greater than unity, the water is supersaturated with precipitated calcium scales. Although the feed solution in the PLA spacer became more concentrated than that without the spacer, with a slightly delayed flux decline, both cases showed a rapid flux drop to zero. However, the CNT spacer was concentrated beyond supersaturation, as can be seen in Fig. 3b, and yet, the water flux was reduced only by 45%. This clearly illustrated the advantage of the CNT spacer, which maximizes water production while not compromising membrane performance due to scaling.

Optical coherence tomography (OCT) was used to identify membrane scaling and fouling on the membrane surface based on the cross-sectional scans³³. The OCT images with respect to VCF during MD operation are shown in Fig. 4. Without any spacer, more dust-like particles, which were scalant, adhered to the membrane

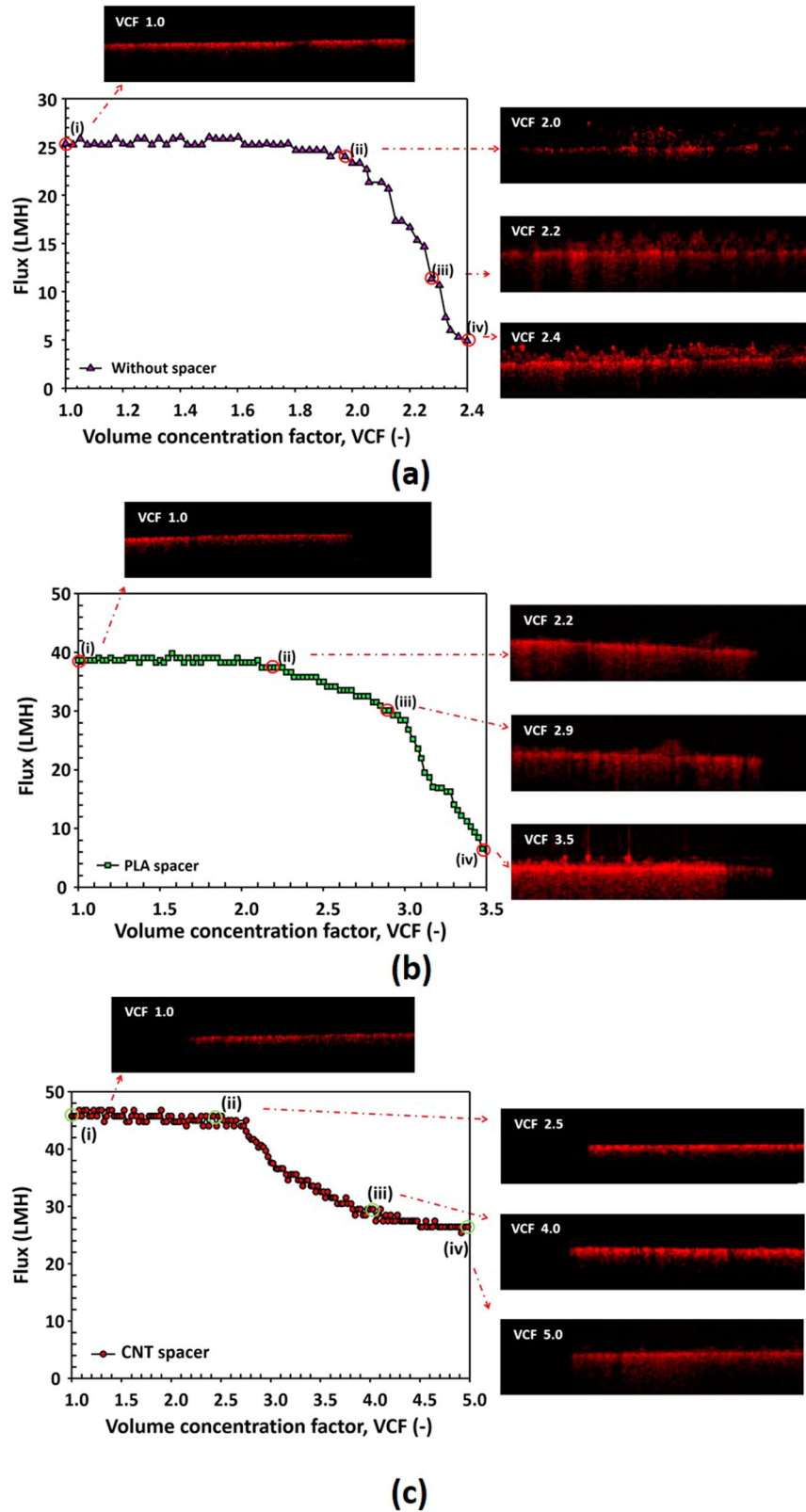


Fig. 4 Optical coherence tomography (OCT) images presenting time-dependent monitoring of cross-section of the membrane. Cross-sectional images of membrane: **a** without spacer, **b** with poly(lactic acid) (PLA) spacer, and **c** carbon nanotube (CNT) spacer. The flow rates of feed and permeate were 0.5 LPM and the concentration of feed solution was initially 0.01 M CaSO_4 . Feed and permeate temperatures were 60 °C and 19.5 °C, respectively.

Table 1. Scaling thickness at VCF 2.4 and after 12 h of MD.

		Without spacer	PLA spacer	CNT spacer
Scaling thickness (μm)	VCF 2.4	30.8 (± 7.1)	10.0 (± 2.0)	None (± 0)
	After 12 h operation*	30.8 (± 7.1)	20.8 (± 5.2)	8.3 (± 4.5)

The flow rates of feed and permeate were 0.5 LPM, and the concentration of feed solution was initially 0.01 M CaSO_4 . Feed and permeate temperatures were 60 °C and 19.5 °C, respectively.

*Without spacer: VCF 2.4, PLA spacer: VCF 3.5, CNT spacer: VCF 5.0.

surface at VCF 2.0 than at VCF 1.0 (Fig. 4a). The scalant stuck on the membrane surface and then grew densely there as the MD progressed. At VCF 2.4, a thicker and denser scaling layer was observed on the membrane surface than at lower VCF. The results of the cross-sectional membrane when the PLA spacer was used are shown in Fig. 4b. The OCT images of the spacers were partially black because the field of view was blocked by the spacer. For the PLA spacer, scalants adhered to the membrane surface were observed after VCF 2.2 and then grew on the membrane densely over time. At VCF 3.5, a much larger and denser scaling layer was formed on the membrane surface. These results indicated that although the PLA spacer retarded membrane scaling to some extent compared to the no-spacer case, it could not completely prevent membrane scaling. The cross-sectional images of the membrane with the CNT spacer are presented in Fig. 4c. Unlike the others, membrane surface scaling was not observed even at VCF 4.0, and a small amount of scalant began to appear on the membrane surface at VCF 5.0. The scaling thicknesses at VCF 2.4 and after 12 h of MD operation are measured and listed in Table 1. At VCF 2.4, the membranes with the PLA spacer and without the spacer were shown 10.0 (± 2.0) and 30.8 (± 7.1) μm scaling thickness, respectively, while using the CNT spacer seemed to hinder the attachment of scalant on the membrane surface. Furthermore, the scaling thickness was measured after MD operation to examine anti-scaling effects in long-term operation, as shown in Table 1. The scaling thicknesses of the membranes with and without PLA spacer were 20.8 (± 5.2) and 30.8 (± 7.1) μm at VCF 3.5 and 2.4, respectively. The scaling thickness of the membrane with the CNT spacer was 8.3 (± 4.5) μm at VCF 5.0. Overall, the measured scaling thickness in different scenarios demonstrated that the CNT spacer effectively retarded membrane scaling.

Membrane characterization

The effects of membrane scaling on the membrane surface during long-term operation (12 h of MD) with and without a spacer are shown in Supplementary Fig. 2. Supplementary Fig. 2a shows the virgin membrane before MD operation. The virgin membrane had a clean white surface. After 12 h of MD operation without a spacer, the membrane surface was contaminated with crystals and turned brown (Supplementary Fig. 2b of the Supplementary Information). Supplementary Fig. 2c shows SEM images of the membranes after 12 h of MD operation with the PLA spacer. The surface of the membrane was clean under the spacer, with no crystals formed. However, crystals still accumulated on the membrane surface outside the regions where the spacer filaments were positioned, i.e., a diamond-shaped spacer pattern of uncontaminated areas. Although the PLA spacer interrupted the build-up of the scalant under the spacer, it did not effectively prevent contamination of the rest of the membrane areas. For the CNT spacer, the membrane surface exhibited a thin crystalline layer after operation, but it was not as contaminated as the other membrane surfaces after 12 h of MD operation (Supplementary Fig. 2d of the Supplementary Information). As a result, the CNT spacer can be considered more effective to maintain the flux high for a long time (Fig. 2).

Moreover, the scaled membranes were further analyzed in terms of water contact angle, indicative of hydrophobicity. This is another indicator that can be used to predict the lifetime of MD

Table 2. Water contact angle (WCA) of membranes after 4 h and 12 h of membrane distillation (MD) operation with 0.01 M of CaSO_4 feed water.

Membrane	4 h		12 h	
	WCA (°)	Membrane	WCA (°)	Membrane
Virgin membrane	111 \pm 4	Virgin membrane	111 \pm 4	
Without spacer (VCF 1.5)	36 \pm 2	Without spacer (VCF 2.4)	-	
PLA spacer (VCF 1.8)	75 \pm 3	PLA spacer (VCF 3.0)	-	
CNT spacer (VCF 2.0)	98 \pm 2	CNT spacer (VCF 5.0)	37 \pm 18	

The flow rates of feed and permeate were 0.5 LPM. Feed and permeate temperatures were 60 °C and 19.5 °C, respectively.

membranes. Table 2 lists the results of the WCA measurements for different cases. The WCA of the virgin membrane before MD operation was 111 \pm 4°, meaning the membrane was initially hydrophobic. In the absence of spacers, after a 4 h operation, the WCA was decreased to 36 \pm 2°, resulting in diminished hydrophobicity, and then became immeasurable after 12 h of MD operation, that is, complete loss of hydrophobicity. The membrane with the PLA spacer was shown to have a WCA of 75 \pm 3° after 4 h of MD operation. However, its hydrophobicity could not be measured after 12 h of operation. After 4 and 12 h of MD operation using the CNT spacer, the values were 98 \pm 2° and 37 \pm 18°, respectively. This indicates that the membrane in the presence of the CNT spacer was able to retain hydrophobicity for a longer time than the other cases.

Figure 5 shows the SEM images of the membrane surface before and after the MD operation in the scaling study. Figure 5a–e are images of the membrane surface captured every 2 h from 4–12 h of MD operation without any spacer. The attached crystals are clearly visible on the membrane surface, as shown in Fig. 5a, with large and small crystals entangled on the membrane surface over time. It can be inferred from the images that small crystals are formed on the membrane surface first, and subsequently, other crystals present in the bulk adhere to the first-generation crystals already established on the membrane surface. As a result, the size of the scaling can grow larger via the build-up of crystals on the surface. After 10 h of operation, most of the membrane surface was covered with crystals (Fig. 5d). Moreover, it was difficult to observe the pores on the membrane surface after 12 h of MD operation because scaling blocked the membrane pores and formed a scaling layer on the membrane surface (Fig. 5e). Figure 5f–j were images of the membrane surface over time in the MD process for the PLA spacer. This is similar to the results of the no-spacer case; however, the amount of scalant attached to the membrane surface was less than that of the membrane without a spacer (Fig. 5a, b, f, g). Images of the membrane surface with the CNT spacer are presented in Fig. 5k–o. Here, small fragments of crystals were observed on the membrane surface, but the crystals did not appear to form a chunk before 8 h of MD operation. After 10 h of operation, crystals were observed on the membrane

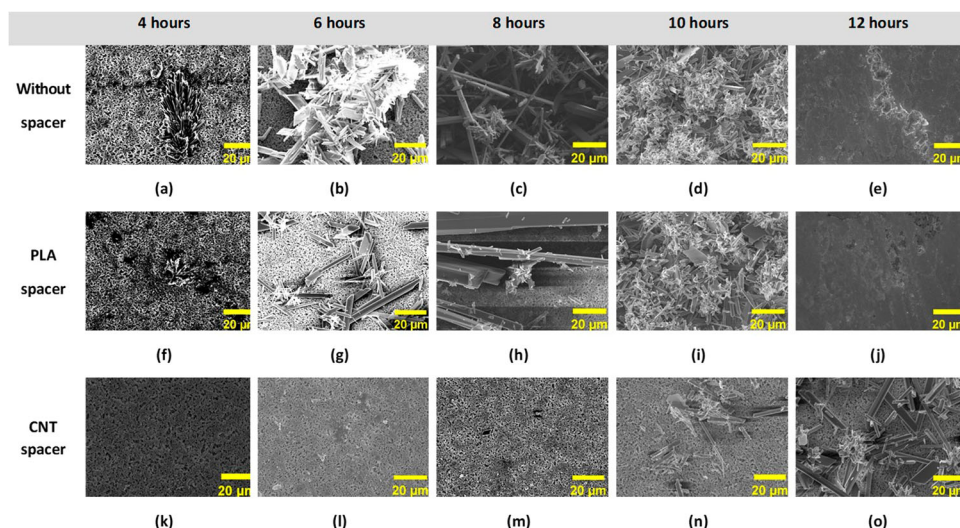


Fig. 5 Scanning electron microscope (SEM) images of the membrane surface measured every 2 h from 4–12 h of operation (magnitude 1000). The membrane **a–e** without spacer, **f–j** with poly(lactic acid) (PLA) spacer, and **k–o** with carbon nanotube (CNT) spacer. The flow rates of feed and permeate were 0.5 LPM and the concentration of feed solution was 0.01 M CaSO_4 . Feed and permeate temperatures were 60 °C and 19.5 °C, respectively.

surface and became larger than those observed even in the initial stage in the no-spacer and the PLA spacer (Fig. 5a, f). This result suggests that the CNT spacer might disrupt the attachment of the scalant to the membrane surface such that the crystals grew extensively in the bulk feed water. In terms of the crystal sizes in the feed water, the crystals were larger in the presence of the CNT spacer than those in the other cases (Supplementary Fig. 3). Supplementary Fig. 4 shows the results of energy dispersive X-Ray spectrometer (EDS) mapping of the membrane surface after MD operation. As a result, it was confirmed that the scaling of the membrane was caused by CaSO_4 , and as expected, the membrane using the CNT spacer showed significantly less scaling than the membrane without a spacer. The CNT spacer also delayed the clogging of the membrane pores with crystals, presumably because the large crystals of the membrane with the CNT spacer were weakly bound and detached more easily than the crystals formed without a spacer or with a PLA spacer.

Mechanism

When the MD was operated in the presence of the CNT spacer with a feed CaSO_4 solution at 0.01 M for a long time (12 h) to allow the membrane scaling, an interesting phenomenon was observed. As shown in Fig. 6 and Supplementary Fig. 5, bubbles were generated on the feed side, especially when feed spacers were present. The use of the PLA spacer resulted in the formation of bubbles predominantly on the membrane surface; however, the appearance of bubbles was not significant. However, for the CNT spacer, much more bubbles were observed in the feed channel. Table 3 presents the count of bubbles observed during 1 h of MD operation.

Figure 6 shows a clear difference in the bubbles formed in the presence of the PLA and CNT spacers at 1 and 12 h. When using the PLA spacer, some bubbles were observed from the beginning of the operation; however, they disappeared over time (Fig. 6a, b). In contrast, the CNT spacer scenario showed several bubbles at the beginning of the operation, and after 12 h of operation, more and larger bubbles were observed compared to the initial first-hour operation (Fig. 6c, d). This was probably because the vaporization rate was enhanced by the increased flux with the CNT spacer. Several studies reported that an increase in the vaporization rate on a heterogeneous surface results in the formation of bubbles³⁴. Furthermore, it has been reported that

rough surfaces can contribute to large bubbles^{35,36}. The generated bubbles flowed along the membrane surface and returned to the feedwater tank. As the MD continued, the number of bubbles passing through the MD module increased, as shown in Fig. 6d. As a result, the generated bubbles could alter the near-wall flow patterns, reducing concentration polarization and scaling on the MD membrane.

To identify the descaling effect of bubbles on the scaling reduction, an additional test was performed with a PLA spacer in the presence of artificial bubbles using an aeration pump. Apart from injecting the excessive number of artificial bubbles, the same operating conditions were used as in the previous experiments. Figure 7b displays the experimental data for the PLA spacer with artificial bubbles. It turned out that bubbles made the initial flux and flux declining rate comparable to the CNT spacers with the naturally generated bubble condition, as shown in Fig. 7b. When the artificial bubbles were injected, the permeate flux was higher than that with the PLA spacer. As explained earlier, this was because bubbles could induce the formation of eddies near the membrane surface, leading to mitigating concentration polarization and scaling. In addition, the permeate flux during bubble generation was maintained at high values above 30 LMH, even at VCF 3.5. This suggests that the bubbly flow over the membrane surface interrupted the attachment of the scalant to the membrane surface^{37–39}. In addition, in the presence of artificial bubbles, the membrane surface was quite clean after the MD operation, as the bubbles improved fluid mixing near the membrane and reduced the scaling effect. Consequently, these results help to understand why the CNT spacer exhibits the distinguished scaling behavior from the PLA spacer or in the absence of spacers. However, it is not possible to completely explain the observed behavior of the CNT spacers using the bubble effects alone; first, even with the number of bubbles excessively and artificially created by the aeration pump, the CNT spacer outperformed the PLA spacer in terms of the higher initial flux, slower flux decline and higher VCF, albeit slightly. Second, there is a subtle difference in the flux decline trend; in the CNT spacer, the flux decline can be roughly divided into two phases: a linear decline with a relatively large slope and a sluggish decline with almost constant flux, as shown in Fig. 2a or Fig. 9c. This flux's biphasic behaviors are not demonstrated by the PLA spacers with artificial bubbles. Therefore, an additional hypothesis was needed

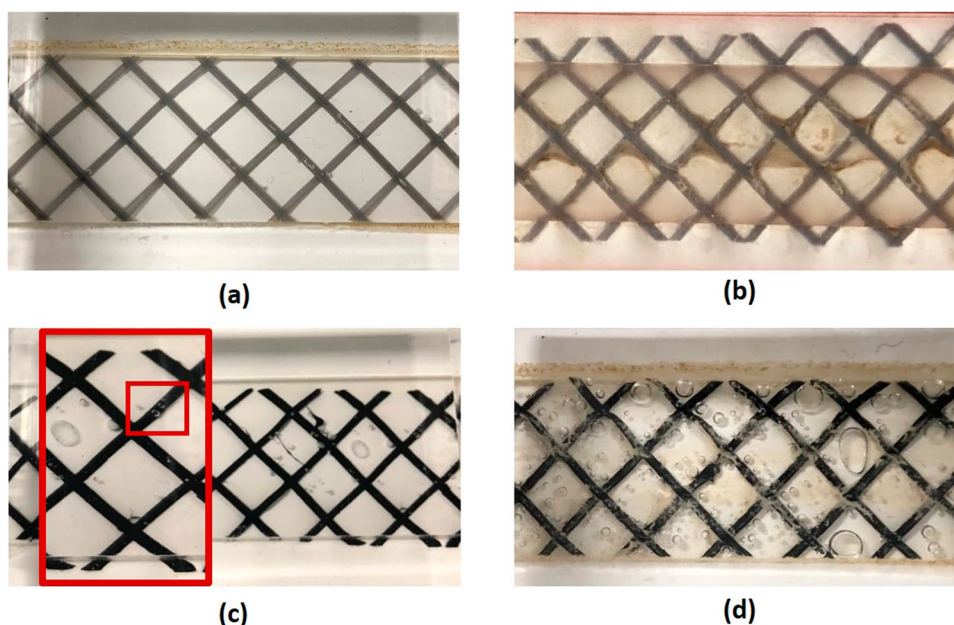


Fig. 6 Generation of bubbles on membrane surface. The membrane images: **a** with poly(lactic acid) (PLA) spacer after 1 h, **b** with PLA spacer after 12 h, **c** with carbon nanotube (CNT) spacer after 1 h, and **d** with CNT spacer after 12 h. The flow rates of feed and permeate were 0.5 LMH, and the concentration of feed solution was 0.01 M CaSO₄. Feed and permeate temperatures were 60 °C and 19.5 °C, respectively.

Table 3. The number of bubbles observed after 1 h of membrane distillation (MD) operation.

	Without spacer	PLA spacer	CNT spacer
Number of Bubble	None (± 0)	3 (± 0)	41 (± 0)

The flow rates of feed and permeate were 0.5 LPM and the concentration of feed solution was initially 0.01 M CaSO₄. Feed and permeate temperatures were 60 °C and 19.5 °C, respectively.

to explain the CNT spacer's improved anti-scaling performance compared to the conventional PLA spacer.

It is widely known that the surface roughness enhances secondary nucleation⁴⁰. Furthermore, at relatively low flow velocities, scaling characteristics are associated with surface characteristics such as wettability and surface energy⁴¹. Also, a recent study on scaling reported the role of hydrodynamics and surface morphology on scale attachment and detachment⁴². These studies motivated us to apply the crystallization theory to our MD system and to build a theoretical model for the crystallization-MD process in order to suggest the second hypothesis and test it by comparing the modeling results with the experimental data.

The crystallization phenomena combined with MD are illustrated in Fig. 8, where the effects of bubbles and scale attachment and detachment are depicted to explain the crystallization mechanisms in the presence of different spacers. First of all, to elaborate further, in the presence of a PLA spacer, nuclei can be formed on either the membrane or the spacer surfaces. Given that the surface area of spacers is much larger than that of membranes, most nuclei formed adhere to the smooth spacer surface first and then grow from it. Therefore, nucleation and growth on the membrane surface are slower in the presence of a spacer than in its absence. The situation in the CNT spacer was similar to that in the PLA spacer. However, due to the surface roughness of the CNT spacer, the initial nuclei would detach from its surface and be present in the bulk post-detachment. This acted as a seed for secondary nucleation. In addition, the nuclei present

in the bulk would grow into solid crystals, resulting in the reduction of dissolved salts in the solution. Simultaneously, water was continuously lost because of membrane permeation. The complementary effect of the loss of dissolved salts and water resulted in a relatively constant water flux at a later stage (Fig. 9c for all temperatures). Nonetheless, membrane surface scaling (i.e., nucleation and growth at the membrane surface) was still in progress, albeit slowly. Therefore, there was a slow decline in water flux. As a result of the parameter estimation procedure, it turns out that the CNT spacer tended to have smaller membrane nucleation rate constants than the PLA spacer. By contrast, the spacer nucleation rate constants for the CNT spacer were higher than those for the PLA spacer.

Figure 9 shows a comparison of the experimental and model calculations, where the symbols and solid lines are experimental data and simulated results, respectively. It can be observed that the model calculations exhibited similar trends of water flux decline over the VCF as those of the experimental results for all tested conditions. The values of the model parameters are presented in Section B.3 of Supplementary Information, along with the results of parametric study that can help to understand the physical meaning of each parameter.

The resultant delayed flux decline is noticeable at a temperature of 60 °C by comparing the blue lines in Fig. 9a, b. The values of the nucleation rate constants for the two cases (without spacer vs. with PLA spacer) at a temperature of 60 °C are also consistent with the hypothesis of competing nucleation from membranes and spacer surfaces (refer to Supplementary Table 1 of the Supplementary Information for parameter values). An interesting finding is that in the absence of a spacer at 60 °C, that is, the lowest temperature tested in this work, the water flux was maintained relatively constant up to a VCF 2 and then gradually decreased to zero. However, as the temperature increased to 70 and 80 °C, the fluxes plummeted at high VCF values, approximately at 1.9 and 1.4, respectively. This could be because as the temperature increased, both growth and nucleation were enhanced in addition to increased concentration rate due to the increased loss of water, especially in the CaSO₄ solution, where the solubility did not vary significantly with temperature. This was also corroborated by the increased values of the estimated growth and nucleation rate

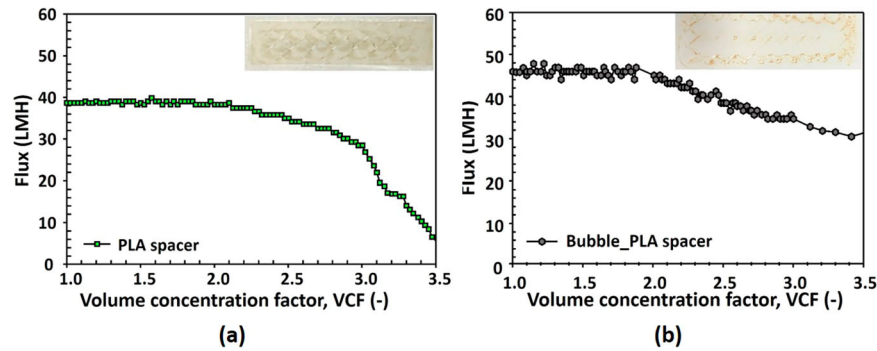


Fig. 7 Comparison of flux and scaling effects on the membrane surface by bubbles in MD operation. a polylactic acid (PLA) spacer and **b** bubbles generated by PLA spacer. The flow rates of feed and permeate were 0.5 LPM and the concentration of feed solution was 0.01 M CaSO₄. Feed and permeate temperatures were 60 °C and 19.5 °C, respectively.

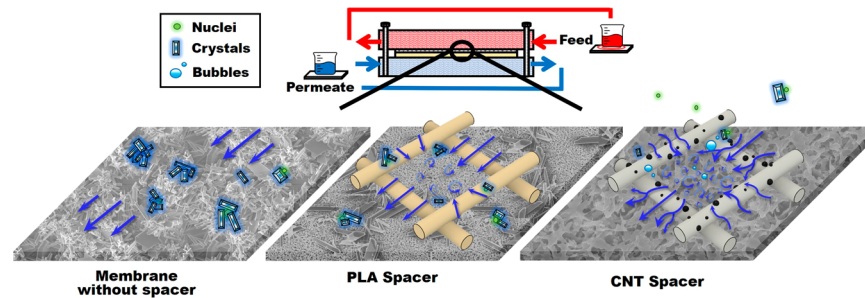


Fig. 8 Schematic of scaling mechanism in the presence of spacers hypothesized in this study. Nucleation took place on three types of surfaces: membrane, spacer and crystals.

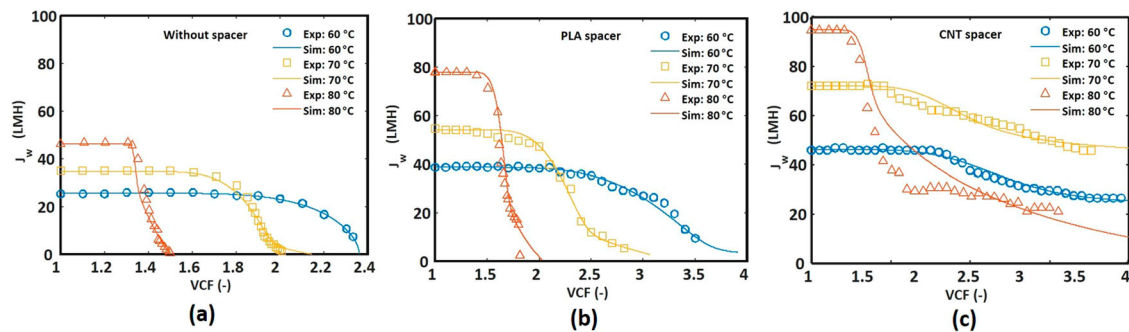


Fig. 9 Comparison between the experimental and simulation results. Water fluxes with respect to VCF for different spacers and feed temperatures: **a** in the absence of a spacer, **b** with polylactic acid (PLA) spacer, and **c** with carbon nanotube (CNT) spacer. The circles, squares, and triangles are experimental data at the feed temperature of 60, 70 and 80 °C, respectively. Solid lines in blue, orange and yellow are simulation results for the feed temperature of 60, 70 and 80 °C, respectively.

constants at high temperatures (see Supplementary Table 1 in the Supplementary Information). Therefore, it can be said that the estimated values of parameters comprising the mechanistic model of the MD-crystallization process partly corroborate the hypothesis of competing crystallization action on the membrane and spacer surfaces and the effects of surface roughness on crystallization to some extent.

Nonetheless, it should be noted that the results of the parameter estimation are based on water flux data over time, rather than on fundamental crystallization experiments, which implies that the set of parameters found in this study might not be unique. That is, parameters should be further fine-tuned based on fundamental crystallization experiments since the parameters found in this work are simply one of the possible parameters that can minimize the squared sum of relative errors between the experimental flux and calculation data. In the future, well-controlled experiments should be designed to independently

identify the nucleation mechanisms at the membrane surface, PLA and CNT spacer surfaces, scaled surfaces (i.e., nucleation from crystals), and bulk crystallization. This allowed us to fine-tune the model parameters separately for each distinct mechanism and analyze the simulation results and model parameters in a more quantitative and reliable manner.

Furthermore, the impact of bubbles formed by improved vaporization rate on crystallization, especially near the membrane surfaces, is not taken into consideration in the developed model. This can be done in the future via coupling of multiphase computational fluid dynamics and crystallization model for a more realistic representation of the experimental set-up and optimization of spacer configuration and operating conditions towards a long-term high-performance MD system⁴³. By doing so, the model can be used to understand the interplay of various factors present in a spacer-embedded MD system for flux enhancement and anti-fouling effects.

METHODS

Membrane

A commercial hydrophobic polyvinylidene fluoride (PVDF, Durapore®, Germany) membrane was used. The pore size and effective area of the membrane were 0.22 μm and 0.0009 m^2 , respectively. The porosity and thickness were 70% and 125 μm , respectively.

3D printing of carbon nanotube-embedded spacer

The CNT-embedded spacer was fabricated using the same methods in our previous study²⁰. The optimal spacer design was found to be 1 mm thickness, 45° filament angle, and 4 mm filament arrangement interval in the previous study, where various combinations of such design parameters were tested and compared to identify the “best” design. These design parameters were selected in terms of the quantity and quality of the produced water (MPF and IRE)²⁰. For details, it is recommended for the readers to refer to our previous work. The spacer was firstly printed into 10 × 4 cm size and then cut into 6.0 × 1.5 cm for the MD operation.

Feed solution

An aqueous solution of CaSO_4 at 0.01 M was used as the feed to replicate scaling formation on the MD membrane. It was prepared by dissolving 1900 mg CaSO_4 ($\text{CaSO}_4 \cdot 2\text{H}_2\text{O}$, Daejung, Republic of Korea) in 1 L deionized (DI) water and stirred at 300 rpm for 1 day before the experiments to make sure of complete dissolution. The solubilities of CaSO_4 were 0.255 and 0.244 g/100 mL at 20 and 60 °C, respectively³¹.

Direct contact membrane distillation set-up and operating conditions

Poly (methyl methacrylate) was used to create a transparent MD module with a window for OCT observation. The feed channel dimensions were 0.015 × 0.06 × 0.002 m (L × W × H). Two gear pumps (EMS-4000, EMS Tech, Republic of Korea) were used to maintain the flow rates at 0.5 L/min (LPM) on both feed and permeate sides. Here, 0.5 LPM was selected to be operated in laminar flow mode, allowing the scalants to deposit on the membrane stably. To assess the effect of feed temperature, the feed solution was heated up to 60, 70, and 80 °C using a hot plate (RCT basic, IKA, Germany) connected to a temperature sensor (PT 1000.60, IKA, Germany), while permeate temperature was kept constant at 19.5 ± 0.5 °C by using a circulating chiller (RW3-0525, Jeio Tech, Republic of Korea). For comparison with the same transmembrane velocity conditions, the feed temperature was set to 60, 65, and 80 °C (CNT spacer, PLA spacer and without spacer, respectively). By doing so, the initial flux was fixed to be approximately 45 LMH in the absence of spacers and in the presence of either spacer. To avoid sedimentation of the scalants in the feed container, the feed solution was continuously stirred at 200 rpm using a magnetic stirrer during the course of MD operation. The permeate water was weighed continuously using an electronic balance (PR4202KR/E; Ohaus, USA) with a resolution of 0.01 g, and data were automatically recorded into a computer every 1 min. The recorded data were used to calculate the permeate flux (J in $\text{Lm}^{-2}\text{h}^{-1}$ or LMH), and all tests were repeated at least three or five times to ensure reproducibility. The results were compared for concentration, scaling level and flux according to the volume concentration factor (VCF). The concentration required to form CaSO_4 scaling was estimated using the saturation ratio (SR) calculated by the following equation^{44,45}:

$$SR = \frac{a_{Me} \cdot a_{An}}{K_{sp}} \quad (1)$$

where a_{Me} and a_{An} are the concentrations of cations and anions in the solution, respectively. K_{sp} is the solubility product under the experiment condition.

The permeate flux J ($\text{Lm}^{-2}\text{h}^{-1}$, LMH) was calculated using the following equation:

$$J = \frac{Q}{A \times t} \quad (2)$$

where Q is the volume of permeated water (L), A the effective membrane area (m^2) and t the time (h).

Characterization of membrane scaling

WCA is an indicator of membrane hydrophobicity. Membrane scaling results in a loss of membrane hydrophobicity; therefore, the WCA can be an indirect indicator of the degree of membrane scaling. WCA was measured using a CA measuring device (Phoenix10, SEO, Republic of Korea) with deionized (DI) water. After the MD test, the surface of the scaled membrane was dried at 24 ± 1 °C overnight prior to WCA measurement. A needle was used to drop DI water onto the dried membrane surface. WCA was reported using the average of five readings taken at different points on the membrane sample to ensure the representativeness of the entire sample.

An image of the membranes after 12 h of MD operation was captured using a cellular phone camera (iPhone 14, Apple). In addition, to observe the scale formation on the membrane surface in detail, SEM (SUPRA40VP, Zeiss, Germany) and energy dispersive X-ray spectrometer (EDS, X-Max EDS detector, Oxford Instruments, UK) were used. To confirm the scaling mechanism, the membrane was also observed every 2 h during MD operation, facilitating the identification of scale formation patterns over time. The scaled membranes were dehydrated overnight at 24 ± 1 °C after MD testing. Subsequently, the dried membrane was mounted on flat plates and coated with platinum (Pt) to prevent electron charging during imaging. SEM images were captured at an accelerating voltage of 10 kV and 1000 × magnification.

Optical coherence tomography (OCT) was used to observe the cross-sectional membrane⁴⁶. In this study, an OCT (OQ Labscope 2.0, Lumedica, USA) device was used to monitor the real-time scale formation and obtain the actual thickness of the scale formed on the membrane. It was equipped with a scan lens fixed to the top of the MD module to monitor the cross-sectional membrane during MD. To observe the scaling phenomenon through the OCT lens, a module with a monitoring window was used. It was placed at the top of the feed channel of the MD module. The 2D cross-sectional OCT scans (512 × 512 pixels) were obtained within a fixed area of 1.0 × 1.0 mm. Scans were periodically obtained during the MD operation. The obtained cross-sectional scans were further processed using the ImageJ software (Sun Microsystems, USA). The images were filtered by reducing noise and adding color. Contrast and brightness were also adjusted. After the image processing, the scaling thickness was measured using a ratio of the number of pixels to actual thickness, and 1 pixel was 2 μm .

During the MD operation, flow images of the membrane were captured using a cellular phone camera (iPhone 14, Apple). Notably, bubbles were observed during MD operation with the CNT spacer. To confirm the effect of bubbles on scale formation, artificial bubbles were injected during the 12 h of MD operation using an air pump (DK-9000, Dae-kwang Electronics, Republic of Korea).

Mathematical modeling of scaling mechanism in MD

We attempted to illustrate the scaling mechanism in DCMD using the crystallization theory. It is initially assumed that secondary nucleation is more dominant than primary nucleation; that is, most nuclei are formed either on the pristine or scaled surfaces of the membrane and spacer because primary nucleation requires significant energy⁴⁷. Secondary nucleation can also be triggered by crystals present in the bulk. Bulk-phase crystallization can occur both on the membrane module and in the feed tank (bulk), where the concentrate from the membrane module is recycled.

Depending on the surface roughness, nuclei may detach from their original sites into the bulk phase. The nuclei in the bulk and on the surface grew into larger crystals.

The bulk concentration of the feed stream varies depending on the crystal formation, growth pattern and water permeation (flux) through the membrane. Water fluxes through the membrane concentrate the feed stream, whereas crystal formation contributes to a reduction in the solution concentration. Therefore, the rate of flux decline was determined by the rates of water permeation, crystal nucleation and growth. Furthermore, crystallization on the membrane surface adversely affects water permeation because it reduces the effective membrane area for water permeation.

We started with a simple population balance equation to describe the crystallization process, assuming a well-mixed system for the MD module and feed tank^{48,49}.

$$\frac{\partial f(t, L)}{\partial t} + \frac{\partial G(t, L)f(t, L)}{\partial L} = F_{in}f_{in} - F_{out}f(t, L) \quad (3)$$

where f is the population density, t the time, L the characteristic length, G the growth rate, F_{in} the inlet flow rate to the MD module, f_{in} the population density in the inflow stream and F_{out} the outlet flow rate from the MD module. For simplicity, it was assumed that the birth and death of crystals owing to breakage or agglomeration were negligible; that is, nucleation is the main mechanism for crystal birth.

By assuming that the growth rate G is not dependent on L , Eq. (3) becomes

$$\frac{\partial f(t, L)}{\partial t} + G(t, L)\frac{\partial f(t, L)}{\partial L} = F_{in}f_{in} - F_{out}f(t, L) \quad (4)$$

Initial and boundary conditions are required to solve Eq. (4), where the nucleation rate is incorporated as part of the boundary condition.

$$f(t, 0) = \frac{B(t)}{G(t, 0)} \quad (5)$$

$$f(0, L) = f_{seed}(L) \quad (6)$$

where B is the nucleation rate and f_{seed} the seed population density.

The moment method can be used to relate population density to a change in concentration in the liquid phase. The q -th moment is defined as follows:

$$\mu_q = \int_0^\infty L^q f(t, L) dL \quad (7)$$

where μ_q is the q -th moment; in particular, the second and third moments can be correlated to the area and volume of crystals, respectively, i.e., the scaled area of membrane and spacer and crystal mass in the bulk and tank for the scaling mechanism in the MD process. The time derivatives of the 0-th and q -th moments can be obtained using Eq. (4) yields:

$$\frac{d\mu^0}{dt} = B(t) + F_{in}\mu_{in}^0 - F_{out}\mu^0 \quad (8)$$

$$\frac{d\mu_q}{dt} = qG(t)\mu_{q-1} \quad (9)$$

By solving for from the 0th to 3rd moments, μ_0 , μ_1 , μ_2 and μ_3 , the areas covered by crystals and crystal mass in the system can be calculated. In the MD, where the retentate is recycled back to the feed tank, crystals can be formed in (i) the feed tank, (ii) the bulk phase in the MD module, (iii) the membrane surface within the MD module, and (iv) the spacer surface within the MD module. Therefore, there are a total of 16 time-variant moments that need to be resolved, $\mu_{q,t}^b$, $\mu_{q,m}^b$, $\mu_{q,s}^b$ and $\mu_{q,t}^s$ with the subscript q being 0–3 and the superscripts t , b , m and s denoting the tank, bulk in the module, membrane and spacer, respectively. The critical terms for

the nucleation and growth rates, $B(t)$ and $G(t)$ can be expressed as a function of the degree of supersaturation.

$$B(t) = k_n \Delta c^\beta \quad (10)$$

$$G(t) = k_g \Delta c^\alpha \quad (11)$$

where k_n is the nucleation rate constant, β the nucleation order, k_g the growth rate constant, α the growth rate order and Δc the supersaturation defined as $c - c^*$ with c^* being the saturated concentration at the corresponding temperature. Finally, the solute mass dissolved in the feed solution was related to the 3rd moments obtained by solving Eqs. (8) and (9), respectively. The detailed model equations and solution procedures are provided in the Supplementary Information (Sections B.1 and B.2).

The developed model involves several model parameters to describe crystallization in the MD module; therefore, experimental data of water fluxes were used to estimate the model parameters. Unfortunately, measurements of such variables as temporal salt concentrations were not available in the current experimental settings, which is crucial for validation and parameter estimation for a dynamic model. More importantly, the amount of crystals presents in the bulk, on the membrane surface and each spacer could not be easily and accurately measured in the integrated system of feed recirculation and the presence of membranes and spacers altogether. Therefore, the hypothesis on the enhanced anti-scaling effects in the CNT spacer (i.e., the effects of spacer surface roughness on enhanced secondary nucleation and scale attachment-detachment) was only partially validated, even though a good agreement between the measured and computed water fluxes over VCF was demonstrated. Although the developed model for integrated MD and crystallization includes several assumptions for simplicity, the mechanistic modeling approach can help to interpret the experimental observations associated with the scaling mechanism in the absence of spacers and in the presence of different spacers. Furthermore, by comparing the values of the key model parameters with physical meanings for different cases, it was possible to identify the dominant step in the crystallization for each experimental case.

DATA AVAILABILITY

The authors confirm that the data supporting the findings of this study are available within the article and its Supplementary materials.

Received: 19 September 2023; Accepted: 6 December 2023;

Published online: 21 December 2023

REFERENCES

- Martínez-Díez, L. & Vázquez-González, M. I. Temperature and concentration polarization in membrane distillation of aqueous salt solutions. *J. Membr. Sci.* **156**, 265–273 (1999).
- Kuang, Z., Long, R., Liu, Z. & Liu, W. Analysis of temperature and concentration polarizations for performance improvement in direct contact membrane distillation. *Int. J. Heat. Mass Transf.* **145**, 118724 (2019).
- Anvari, A., Kekre, K. M. & Ronen, A. Scaling mitigation in radio-frequency induction heated membrane distillation. *J. Membr. Sci.* **600**, 117859 (2020).
- Chen, L. & Wu, B. Research progress in computational fluid dynamics simulations of membrane distillation processes: a review. *Membranes* **11**, 513 (2021).
- Alsaadi, A. S., Francis, L., Amy, G. L. & Ghaffour, N. Experimental and theoretical analyses of temperature polarization effect in vacuum membrane distillation. *J. Membr. Sci.* **471**, 138–148 (2014).
- Manawi, Y. M., Khraisheh, M. A. M. M., Fard, A. K., Benyahia, F. & Adham, S. A predictive model for the assessment of the temperature polarization effect in direct contact membrane distillation desalination of high salinity feed. *Desalination* **341**, 38–49 (2014).
- Bahmanyar, A., Asghari, M. & Khoobi, N. Numerical simulation and theoretical study on simultaneously effects of operating parameters in direct contact membrane distillation. *Chem. Eng. Process. Process Intensif.* **61**, 42–50 (2012).

8. Naidu, G., Zhong, X. & Vigneswaran, S. Comparison of membrane distillation and freeze crystallizer as alternatives for reverse osmosis concentrate treatment. *Desalination* **427**, 10–18 (2018).
9. Kayvani Fard, A. et al. Reducing flux decline and fouling of direct contact membrane distillation by utilizing thermal brine from MSF desalination plant. *Desalination* **379**, 172–181 (2016).
10. Song, Y., Qin, W., Li, T., Hu, Q. & Gao, C. The role of nanofiltration membrane surface charge on the scale-prone ions concentration polarization for low or medium saline water softening. *Desalination* **432**, 81–88 (2018).
11. Tijting, L. D. et al. Fouling and its control in membrane distillation—a review. *J. Membr. Sci.* **475**, 215–244 (2015).
12. He, F., Sirkar, K. K. & Gilron, J. Studies on scaling of membranes in desalination by direct contact membrane distillation: CaCO₃ and mixed CaCO₃/CaSO₄ systems. *Chem. Eng. Sci.* **64**, 1844–1859 (2009).
13. Elcick, H. et al. Multi-effect distillation brine treatment by membrane distillation: Effect of antiscalant and antifoaming agents on membrane performance and scaling control. *Desalination* **493**, 114653 (2020).
14. Christie, K. S. S., Yin, Y., Lin, S. & Tong, T. Distinct behaviors between gypsum and silica scaling in membrane distillation. *Environ. Sci. Technol.* **54**, 568–576 (2020).
15. Warsinger, D. M., Swaminathan, J., Guillen-Burrieza, E. & Arafat, H. A. Scaling and fouling in membrane distillation for desalination applications: a review. *Desalination* **356**, 294–313 (2015).
16. Song, L., Li, B., Sirkar, K. K. & Gilron, J. L. Direct contact membrane distillation-based desalination: novel membranes, devices, larger-scale studies, and a model. *Ind. Eng. Chem. Res.* **46**, 2307–2323 (2007).
17. Rolf, J. et al. Inorganic scaling in membrane desalination: models, mechanisms, and characterization methods. *Environ. Sci. Technol.* **56**, 7484–7511 (2022).
18. Chang, H., Hsu, J.-A., Chang, C.-L., Ho, C.-D. & Cheng, T.-W. Simulation study of transfer characteristics for spacer-filled membrane distillation desalination modules. *Appl. Energy* **185**, 2045–2057 (2017).
19. Phattaranawik, J., Jiratananon, R. & Fane, A. G. Effects of net-type spacers on heat and mass transfer in direct contact membrane distillation and comparison with ultrafiltration studies. *J. Membr. Sci.* **217**, 193–206 (2003).
20. Jeong, S. et al. Engineered multi-scale roughness of carbon nanofiller-embedded 3D printed spacers for membrane distillation. *Water Res.* **231**, 119649 (2023).
21. Kyoungjin An, A. et al. Enhanced vapor transport in membrane distillation via functionalized carbon nanotubes anchored into electrospun nanofibres. *Sci. Rep.* **7**, 41562 (2017).
22. Tijting, L. D. et al. Superhydrophobic nanofiber membrane containing carbon nanotubes for high-performance direct contact membrane distillation. *J. Membr. Sci.* **502**, 158–170 (2016).
23. Roy, S., Bhadra, M. & Mitra, S. Enhanced desalination via functionalized carbon nanotube immobilized membrane in direct contact membrane distillation. *Sep. Purif. Technol.* **136**, 58–65 (2014).
24. Bhadra, M., Roy, S. & Mitra, S. Flux enhancement in direct contact membrane distillation by implementing carbon nanotube immobilized PTFE membrane. *Sep. Purif. Technol.* **161**, 136–143 (2016).
25. Noy, A. et al. Nanofluidics in carbon nanotubes. *Nano Today* **2**, 22–29 (2007).
26. Humoud, M. S., Roy, S. & Mitra, S. Scaling reduction in carbon nanotube-immobilized membrane during membrane distillation. *Water* **11**, 2588 (2019).
27. Sianipar, M., Kim, S. H., Khoiruddin, K., Iskandar, F. & Wenten, I. G. Functionalized carbon nanotube (CNT) membrane: progress and challenges. *RSC Adv.* **7**, 51175–51198 (2017).
28. Lee, J.-G. et al. Theoretical modeling and experimental validation of transport and separation properties of carbon nanotube electrospun membrane distillation. *J. Membr. Sci.* **526**, 395–408 (2017).
29. Lee, J.-G., Jeong, S., Alsaadi, A. S. & Ghaffour, N. Influence of high range of mass transfer coefficient and convection heat transfer on direct contact membrane distillation performance. *Desalination* **426**, 127–134 (2018).
30. Yin, Y. et al. Contrasting behaviors between gypsum and silica scaling in the presence of antiscalants during membrane distillation. *Environ. Sci. Technol.* **55**, 5335–5346 (2021).
31. Peng, J. et al. Simulation for the dissolution mechanism of Cambrian carbonate rocks in Tarim Basin, NW China. *Pet. Explor. Dev.* **45**, 431–441 (2018).
32. Hoang, T. A., Ang, H. M. & Rohl, A. L. Effects of temperature on the scaling of calcium sulphate in pipes. *Powder Technol.* **179**, 31–37 (2007).
33. Lee, J.-G. et al. An advanced online monitoring approach to study the scaling behavior in direct contact membrane distillation. *J. Membr. Sci.* **546**, 50–60 (2018).
34. Choi, C.-H. et al. Large-scale generation of patterned bubble arrays on printed bi-functional boiling surfaces. *Sci. Rep.* **6**, 23760 (2016).
35. Dhillon, N. S. Effect of surface roughness on the behavior of bubbles growing and departing from a heated surface. ASME Heat Transfer Summer Conference, <https://doi.org/10.1115/HT2017-5113> (2017).
36. Yang, J., Duan, J., Fornasiero, D. & Ralston, J. Very small bubble formation at the solid–water interface. *J. Phys. Chem. B* **107**, 6139–6147 (2003).
37. Ye, Y. et al. Microbubble aeration enhances performance of vacuum membrane distillation desalination by alleviating membrane scaling. *Water Res.* **149**, 588–595 (2019).
38. Ali, M. E. A., Alghanayem, R., Varela, A., Bellier, M. & Perreault, F. Scaling mitigation in direct contact membrane distillation using air microbubbles. *Desalination* **549**, 116348 (2023).
39. Farid, M. U. et al. Nanobubble-assisted scaling inhibition in membrane distillation for the treatment of high-salinity brine. *Water Res.* **209**, 117954 (2022).
40. Grosfils, P. & Lutsko, J. F. Impact of surface roughness on crystal nucleation. *Crystals* **11**, 4 (2021).
41. Jin, H.-Q., Athreya, H., Wang, S. & Nawaz, K. Experimental study of crystallization fouling by calcium carbonate: effects of surface structure and material. *Desalination* **532**, 115754 (2022).
42. Løge, I. A. et al. Scale attachment and detachment: the role of hydrodynamics and surface morphology. *Chem. Eng. J.* **430**, 132583 (2022).
43. Ali, B. A. & Falleiro, L. H. Effect of baffle configuration on performance of batch stirred vessel. *Korean J. Chem. Eng.* **39**, 1146–1157 (2022).
44. Meijer, J. A. M. & Van Rosmalen, G. M. Solubilities and supersaturations of calcium sulfate and its hydrates in seawater. *Desalination* **51**, 255–305 (1984).
45. Bijani, M. & Khamchi, E. Optimization and treatment of wastewater of crude oil desalting unit and prediction of scale formation. *Environ. Sci. Pollut. Res.* **26**, 25621–25640 (2019).
46. Fortunato, L. et al. Fouling development in direct contact membrane distillation: non-invasive monitoring and destructive analysis. *Water Res.* **132**, 34–41 (2018).
47. Agrawal, S. G. & Paterson, A. H. J. Secondary nucleation: mechanisms and models. *Chem. Eng. Commun.* **202**, 698–706 (2015).
48. Costa, C. B. B., Maciel, M. R. W. & Filho, R. M. Considerations on the crystallization modeling: Population balance solution. *Comput. Chem. Eng.* **31**, 206–218 (2007).
49. Rasmuson, Å. C. in *Handbook of Industrial Crystallization*. <https://www.cambridge.org/> (2019).

ACKNOWLEDGEMENTS

This study was funded by two Basic Science Research Programs through the National Research Foundation of Korea (NRF) funded by the Ministry of Education (NRF-2022R1C1C1006877 and NRF-2021R1A6A1A03039572), a National Research Foundation of Korea (NRF) grant funded by the Korean government (MSIT) (No. 2021R1C1C1006287), the Institutional Research Program of Korea Research Institute of Chemical Technology (KRITC) (No. KK2312-30), 2022-2023 BK21 FOUR Graduate School Innovation Support funded by Pusan National University (PNU-Global Fellowship program), and the Korea Institute of Energy Technology Evaluation and Planning (KETEP) grant funded by the Korea government (MOTIE) (20229A10100040, Development of high technology materials processing from electronic wastes by utilizing natural resources).

AUTHOR CONTRIBUTIONS

Seongeom Jeong: investigation, writing - original draft; B.G.: formal analysis, writing - original draft, supervision; S.P.: investigation, writing - review & editing; K.C.: resources, writing - review & editing; A.K.A.: writing - review & editing. Sanghyun Jeong: conceptualization, methodology, writing - review & editing, supervision, funding acquisition.

COMPETING INTERESTS

The authors declare no competing interests.

ADDITIONAL INFORMATION

Supplementary information The online version contains supplementary material available at <https://doi.org/10.1038/s41545-023-00296-0>.

Correspondence and requests for materials should be addressed to Boram Gu or Sanghyun Jeong.

Reprints and permission information is available at <http://www.nature.com/reprints>

Publisher's note Springer Nature remains neutral with regard to jurisdictional claims in published maps and institutional affiliations.



Open Access This article is licensed under a Creative Commons Attribution 4.0 International License, which permits use, sharing, adaptation, distribution and reproduction in any medium or format, as long as you give appropriate credit to the original author(s) and the source, provide a link to the Creative Commons license, and indicate if changes were made. The images or other third party material in this article are included in the article's Creative Commons license, unless indicated otherwise in a credit line to the material. If material is not included in the article's Creative Commons license and your intended use is not permitted by statutory regulation or exceeds the permitted use, you will need to obtain permission directly from the copyright holder. To view a copy of this license, visit <http://creativecommons.org/licenses/by/4.0/>.

© The Author(s) 2023